ChemCatChem

Full Papers
doi.org/10.1002/cctc.201902309

Design and Synthesis of Sm, Y, La and Nd-doped CeO_2 with a broom-like hierarchical structure: a photocatalyst with enhanced oxidation performance

Bin Xu,*[a] Hui Yang,[a] Qitao Zhang,*[b] Saisai Yuan,[c] An Xie,[a] Ming Zhang,[a] and Teruhisa Ohno*[d]

CeO_2 doped with various rare earth (RE) ions (Sm, Y, La and Nd) having a broom-like hierarchical structure was successfully prepared by a template-free hydrothermal method. The photooxidation performance of RE-doped products was significantly better than that of pure CeO_2, and comparative experiments showed that Sm-doped CeO_2 (SC) has superior photooxidation activity, resulting about 3.0-times and 8.5-times higher activities of bisphenol A (BPA) degradation and of acetaldehyde (CH_3CHO) decomposition, respectively, than those of pure CeO_2. Due to the incorporation of RE ions, the surface exposed cerium ions are partly substituted by those cations, resulting in a higher concentration of oxygen vacancies (O_v) in RE-doped CeO_2. The increased O_v can act as a trapping center for photogenerated electrons to form a doping transition state between the conduction band (CB) and valence band (VB), which can restrict the recombination rate of electrons and holes effectively and lead to an outstanding enhancement of photooxidation performance. Furthermore, abundant highly reactive hydroxyl radicals ($^{\bullet}OH$) and superoxide radicals ($^{\bullet}O_2^-$), which are efficient intermediates with vivid oxidation ability, can further enhance the photocatalytic activity of RE-doped CeO_2. A cost-effective strategy for designing CeO_2-based semiconductor photocatalysts doped with multitudinous RE ions that have enhanced photooxidation performance is presented in this paper.

Introduction

Recently, human health and ecosystems have been threatened by a serious threat to environmental pollution mainly due to organic pollutants and toxic gas wastes generated in industrialization process.[1–3] Novel photocatalytic materials for elimination of multi-species pollutants from industrial streams have been developed.[2–4] However, newly developed materials have some problems such as a high rate of recombination of photogenerated electrons and holes, poor photo-chemical stability and weak visible light absorption, which greatly hinder their popularization and application as cost-efficient semiconductor photocatalysts.[2,3]

Cerium dioxide (CeO_2) is one of the most important rare earth metal oxides, and it has attracted much attention due to its excellent properties such as low toxicity, high degree of chemical stability, safety and resistance to photocorrosion primarily.[4] It has various applications including applications as UV blockers, polishing materials, photocatalysts, electrolytes, sensors and fuel cells.[5] In addition, the photocatalytic properties of CeO_2 are similar with those of TiO_2-based materials including a wide band gap (2.90 eV) and strong absorption in the UV region. It is therefore a promising candidate material for photocatalytic degradation of deleterious organic pollutants. Previous studies have shown that morphology and size control, doping of various metal ions, and heterojunction coupling are three common strategies for enhancing the photocatalytic performance of CeO_2-based materials.[5,6] The morphology of CeO_2 plays a major role in its photocatalytic performance, and our research group has successfully fabricated a series of high-performance CeO_2 photocatalysts with different morphologies and superior performances including porous broom-like, hedgehog-like, confeito-like and hollow octahedral structures.[7–9] Difference in morphology and size can determine the specific surface area, active sites and separation of redox crystal facets, which are related to improvement of photocatalytic performance. Choudhury has studied the effect of $[Ce^{3+}]$ and oxygen vacancies on the photocatalytic activity of CeO_2.[10] The large deviated stoichiometry of CeO_2 makes it easier for cerium ions to be reduced from tetravalent cerium to trivalent cerium and enhance the formation of active oxygen vacancies (O_V).[11–13] The

---

[a] Assoc. Prof. B. Xu, H. Yang, Assoc. Prof. A. Xie, Prof. M. Zhang
School of Chemistry and Chemical Engineering
Yangzhou University
Yangzhou, 225009 (P. R. China)
E-mail: twt@yzu.edu.cn
[b] Assoc. Prof. Q. Zhang
International Collaborative Laboratory of 2D Materials for Optoelectronics Science and Technology of Ministry of Education
Institute of Microscale Optoelectronics
Shenzhen University
Shenzhen, 518060 (P. R. China)
E-mail: qitao-zhang@szu.edu.cn
[c] S. Yuan
Department of Chemical and Biochemical for Energy Materials
Xiamen University
Xiamen, 361005 (P. R. China)
E-mail: yuansaisai66666@163.com
[d] Prof. T. Ohno
Department of Applied Chemistry
Faculty of Engineering
Kyushu Institute of Technology
Kitakyushu, 804-8550 (Japan)
E-mail: tohno@che.kyutech.ac.jp

Supporting information for this article is available on the WWW under https://doi.org/10.1002/cctc.201902309

effectiveness of pure CeO_2 also can be improved by introducing foreign metal ions to promote the formation of expanded crystal-structured CeO_2-based products, which are more convenient for electronic transmission.[14] Some studies have indicated that the introduction of various metal dopant such as Fe, Eu and Mn can change the structure and optical properties of CeO_2.[15–17] Studies have also shown that the presence of metal ions in the ceria lattice induced more trivalent ceria ions and oxygen vacancies, which are more important for photocatalytic pollution degradation.[11] The key point of these methods is the change in the oxygen vacancies concentration of the products, which can serve as electron-capture centers.[10] Thus, the as-formed oxygen vacancies can also effectively suppress the recombination of electron-hole pairs, thereby improving the final photocatalytic activity.[16–22] Therefore, doping of foreign ions a cost-effective way to enhance the activity of a CeO_2-based photocatalyst. To the best of our knowledge, it is very difficult to introduce different ions into the lattice of ceria, and there has been no report about a summary of CeO_2 with doping a series of different RE ions and elucidation of the effects on photocatalytic performance systematically.

In this paper, CeO_2 materials doped with several rare earth ions (Sm, Y, La and Nd) that have a broom-like hierarchical structure were prepared by a template-less hydrothermal method. The photooxidation efficiency of the samples were evaluated by experiments on aqueous BPA degradation and on CO_2 evolution from CH_3CHO decomposition. Furthermore, the morphology, structure and photoelectrochemical properties were examined to determine the effect of RE ions doping. Due to an increasing concentration of oxygen vacancies, photooxidation performance of RE-doped products was significantly better than that of pure CeO_2, and the results of comparative experiments showed that Sm-doped CeO_2 has the best photooxidation activity. Thus, doping with appropriate ions is effective for enhancing the photocatalytic activity of a bulk photocatalyst.

Results and Discussion

The morphology of as-prepared products was investigated by FE–SEM and HR–TEM. As exhibited in Figure 1a, pure CeO_2 shows a broom-like hierarchical morphology with a single root length of 5 μm and diameter of 200 nm approximately. Clear lattice fringes with interplanar spacing of 0.313 nm, which are assigned to the CeO_2 (111) crystal plane, can be seen in Figure 1A. After doping with different RE ions, the products still maintain the broom-like hierarchical structure (Figure 1b–e). However, there are distinct changes in the degree of surface smoothness and average diameter and length of the nanorods. It is notable that the lattice fringes in the RE-doped products have interplanar spacing: SC (0.320 nm), YC (0.314 nm), LC (0.328 nm) and NC (0.325 nm) (Figure 1B–E). The alteration in lattice spacing indicates that those RE ions have been successfully introduced into the interior lattice of CeO_2, but the crystal structure of ceria's cubic fluorite is in fact preserved.

EDS mapping results (Figure 2) indicate that only cerium and oxygen elements are clearly detected in pure CeO_2 and are evenly distributed among the nanorods. After the introduction of RE ions, doping elements except for Ce and O also have a good distribution on the surface (Figure 2b–e). In view of the above results, it can be further inferred that photocatalysts doped with different RE ions can be successfully prepared by a hydrothermal treatment.

XRD patterns of as-fabricated samples are shown in Figure 3a. The characteristic diffraction peaks of CeO_2 are located at 28.60°, 33.27°, 47.71° and 56.51°, corresponding to the crystal planes of (111), (200), (220) and (311), respectively.[22,23] All of the diffraction lines can be attributed to the phase of ceria with a cubic fluorite structure (space group: Fm-3 m (225)), which is in accordance with the standard data reported in the JCPDS card (No. 65-5923).[23–24] The sharp diffraction peaks of products suggest a high degree of crystallinity, and no appearance of impurity peaks manifests that doping has a negligible effect on crystal growth. Compared with pure CeO_2, the elaborated XRD patterns (Figure 3b) of the highest (111) peak exhibit an obvious shift to a lower angle after doping. This phenomenon can be conspicuously attributed to the introduction of rare earth ions into the crystal structure.[24] And these results are

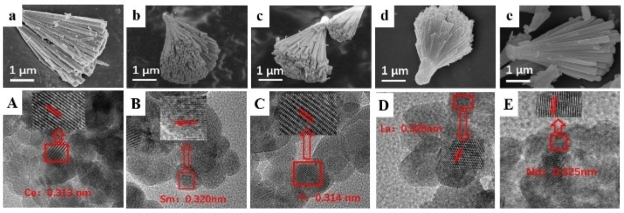

Figure 1. FE–SEM and HR–TEM images: (a, A) CeO_2, (b, B) SC, (c, C) YC, (d, D) LC and (e, E) NC.

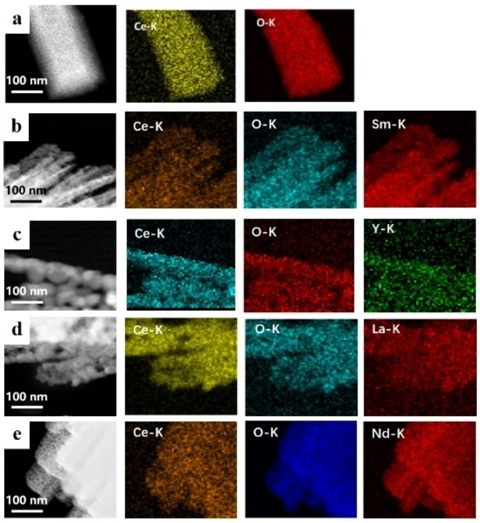

Figure 2. HAADF image and distribution of element mapping images: (a) CeO_2, (b) SC, (c) YC, (d) LC and (e) NC.

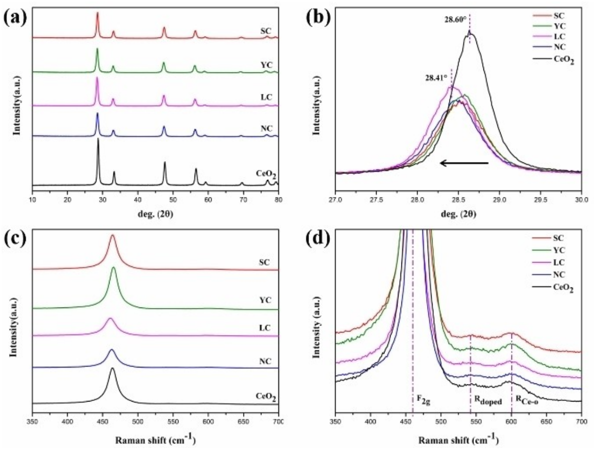

Figure 3. Structure characterization: (a) XRD patterns, (b) detailed view of the highest (111) peak patterns, (c) Raman spectra and (d) enlarged view of Raman spectra.

consistent with the changes in lattice fringes observed in HR–TEM.

Rietveld refinement was further carried out to determine the actual doping location of incorporated ions and the results are summarized in Table S1. It can be clearly seen that the lattice parameter values of RE-doped samples become larger than that of pure CeO_2 (5.4114 Å). The values are 5.4182 Å, 5.4290 Å, 5.4219 Å and 5.4211 Å for SC, YC, LC, and NC, respectively. In comparation to Ce^{4+} (0.970 Å), the enlarged lattice parameters can be attributed to the larger ionic radius of various rare earth element ions such as Sm^{3+} (1.079 Å), Y^{3+} (1.019 Å), La^{3+} (1.160 Å), Nd^{3+} (1.109 Å). In the MO_8 crystal structure of ceria, the substitution reaction is more likely to occur on cerium atoms located on the top and edge than in the body center. When the rare earth ions have been introduced into the crystal structure of CeO_2, its crystal lattice would be greatly expanded. It is well known that an expanded crystal structure is more beneficial than normal MO_8 crystal structure for electronic transmission.[25]

Raman technology is an effective and non-destructive technique for characterizing structural defects.[26] The distinct peak at 460 cm^{-1} is assigned to F_{2g} vibration of the cubic fluorite structure as illustrated in Figure 3c. Two weak Raman peaks located at 540 cm^{-1} and 600 cm^{-1} were also detected, and they are ascribed to extrinsic defects caused by doping (R_{dopant}) and instinctive defect vibration of Ce–O ($R_{Ce\text{-}O}$), respectively.[27–29] An enlarged view of Raman peaks is shown in Figure 3d. According to the results of previous studies,[30] cerium ions show a trivalent state instead of tetravalent chemical valence in the defect lattice partly. In order to maintain the particles in an electrically neutral state, surface oxygen would escape from the structure, eventually resulting in the formation of inherent oxygen vacancies (O_v).[31] Later, more oxygen vacancies would promote the separation of charge carriers and limit the recombination rate of photo-generated carriers. The relative photocatalytic performance would be enhanced. The relativity intensity of a Raman shift of F_{2g}, R_{dopant} and R_{Ce-O} can be calculated from Equation (1):[30,31]

$$\frac{O_V}{F_{2g}}\% = \frac{Aera_{R_{Ce-O}} + Aera_{R_{dopant}}}{Aera_{F_{2g}}}\% \qquad (1)$$

The calculated values are outlined in Table S2. Compared with pure CeO_2, the values of O_v clearly increase after RE ion doping. And the value of O_v reaches a maximum of 12.50% after Sm doping, being consistent with the result of XPS analysis shown below.

The surface chemical composition and the interactions before and after doping were analyzed by XPS spectroscopy (Figure S1 & Figure S2). The Ce3d electron core level and two group peaks obtained (denoted as v and u) after deconvolution treatment are displayed in Figure 4a. According to previous studies,[31,32] the labels of (U, V), (U_2, V_2) and (U_3, V_3) can be classified as Ce $3d_{5/2}$ and Ce $3d_{3/2}$ related to Ce^{4+}, originating from the final states of Ce ($3d^94f^0$) O ($2p^6$), Ce ($3d^94f^1$) O ($2p^5$) and Ce ($3d^94f^2$) O ($2p^4$), respectively. Two pairs of doublets, (U_0, V_0) and (U_1, V_1), for the Ce 3d bond energy peak can be ascribed to Ce^{3+}, and the double lines correspond to Ce ($3d^94f^1$) O ($2p^6$) and Ce ($3d^94f^1$) O ($2p^5$), respectively.[31,32] In order to estimate the concentration of [Ce^{3+}] of samples, these peaks were deconvoluted and the calculated concentration value of as-prepared samples are shown in Table S2. The [Ce^{3+}] ratio is obviously increased after RE ions doping, which is much higher than the product without doping. Meanwhile, the concentration of [Ce^{3+}] of SC is 17.69%, which is the highest among the products of doping. In addition, these peaks significantly shift to a lower binding energy and it manifests that Sm ions indeed dope into the lattice of CeO_2 (Figure 4b). Therefore, it can be understood that the introduction of dopants greatly influences the chemical environment of Ce–O by the reduction of $Ce^{4+} \rightarrow Ce^{3+}$, which is a foremost reason for the increased concentration in oxygen vacancies, which are beneficial for enhancing photocatalytic efficiency when compared with pure CeO_2.[10]

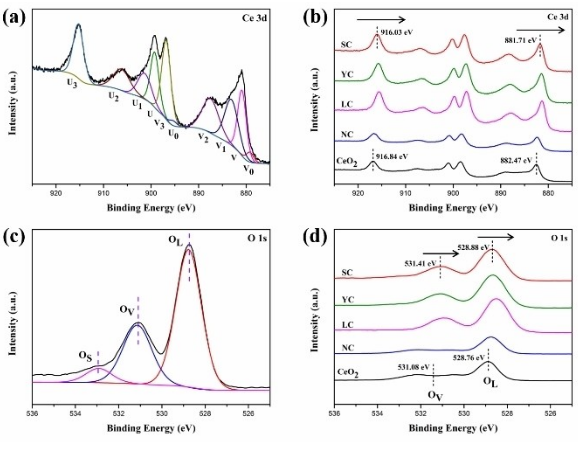

Figure 4. Separated peak curves of (a) Ce 3d, (c) O 1s, high-solution XPS spectra of (b) Ce 3d, and (d) O 1s of all samples.

Three different types of oxygen species, assigned to lattice oxygen (O_{lat}), oxygen vacancies (O_V) and active surface oxygen (O_{Sur}), can be clearly detected after deconvolution of the O1s electron core level located binding energy of 528.76, 531.08, and 532.95 eV, respectively (Figure 4c).[33] The binding energy of these oxygen species significantly shifts towards lower binding energy after doping of RE ions. However, the effects on O_{lat}, O_v and O_{Sur} are quite different. Compared with pure CeO_2, the binding energy value of O_v shows a change of 0.33 eV after Sm doping. The binding energy value of the O_{lat} and O_{Sur} shows changes of only 0.12 eV and 0.20 eV, respectively. (Figure 4d). Therefore, RE ions doping mainly affects the binding energy of O_v. The O_v ratio after deconvolution and multimodal separation is obtained in Table S2. It can be observed that the concentration of $[O_v]$ in doped-CeO_2 is much higher than that in pure CeO_2, while a similar phenomenon exists for $[Ce^{3+}]$. In particular, the concentrations of $[Ce^{3+}]$ and $[O_v]$ in SC are 17.69 % and 15.25 %, respectively, which are significantly higher than other products. It may due to the substitution process can compensate for the charge generated by doping and promote the formation of oxygen vacancies in defective structured CeO_2. And these vivacious O_v, acting as a trapping center for photogenerated electrons, formed a doping transition state between the conduction band (CB) and valence band (VB), and limited the recombination rate of electrons and holes significantly, leading to an outstanding improvement of photooxidation performance effectively.[7] Therefore, it provides a forceful evidence to speculate that RE-doped CeO_2 should have higher photocatalytic activity.[33,34]

Firstly, photooxidation activity of as-prepared products was evaluated by degradation of aqueous bisphenol A (BPA). The BPA removal rate of SC reaches 98.76 % under light irradiation for 6 h (Figure 5a), which is significantly better than that of other samples. The lowest rate constant for photocatalytic degradation activity obtained for the pure CeO_2 is only 34.07 %. According to the kinetic equation (Figure 5b), the rate constant κ value of SC is 0.5145 h^{-1}, and SC possesses 1.32−, 3.31−, 4.31−, and 5.30-times higher than those of YC, LC, NC and pure CeO_2, respectively. Besides, the tendency of $-\text{Ln}\ (C_t/C_0)$ as a function of irradiation time is displayed in Table S3. It can be concluded that the linear relationship between $-\text{Ln}\ (C_t/C_0)$ and irradiation time follows the pseudo-first order kinetic equation, where C_0 is the initial concentration of BPA and C_t is the concentration at a particular time. After numerical calculation, the rate constant indicates that BPA degradation obeys the Langmuir-Hinshelwood rate. For investigating the BPA photocatalytic degradation process, HPLC was used to analyze the products of each stage. The peak of retention time of 7.74 min is mainly attributed to BPA, and the intensity of the peak decreases gradually during the reaction process, indicating that BPA is degraded continuously (Figure S3). A new peak located at a retention time of 4.04 min appears after photodegradation for two hours, corresponding to p-hydroxyacetophenone, and the intensity gradually increases. Therefore, it should be a major degradation product. In addition, a weak peak at 5.09 min belongs to phenol, and its intensity increases with increase in reaction time. The results of HPLC show that p-hydroxyacetophenone and phenol are the main intermediate products during BPA degradation. These inter-mediate products may be further oxidized and decomposed, and the final products are non-toxic CO_2 and H_2O. Hence, the following reaction processes are proposed in Equations (2–4):

$$CeO_2 + h\nu \rightarrow CeO_2\ (h^+) + CeO_2\ (e^-) \tag{2}$$

$$OH^- + h^+ \rightarrow {}^{\bullet}OH \tag{3}$$

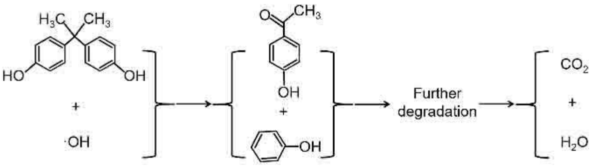

(4)

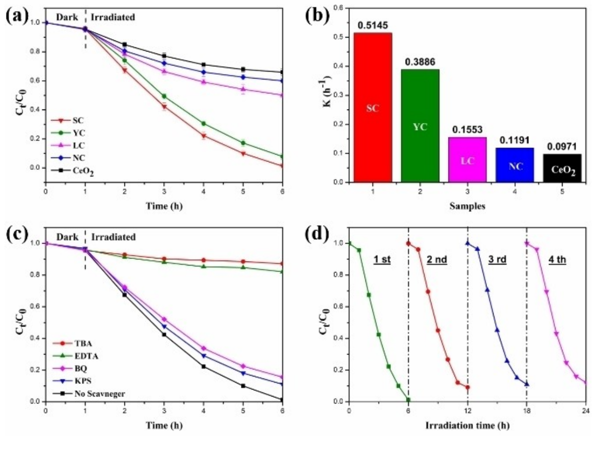

Figure 5. (a) BPA photooxidation degradation curves, (b) degradation kinetics constants, (c) degradation efficiency with the addition of scavengers and (d) stability test.

The BPA degradation pathways have already been established, and it is also necessary to identify the main active substance in the degradation process by trapping experiments.[35,36] As demonstrated in Figure 5c, the photodegradation efficiency of BPA decreases rapidly from 98.76 % to 12.83 % after adding TBA, indicating that $^{\bullet}OH$ is one of the main active species in the BPA photodegradation process. When EDTA was added, the degradation efficiency was also reduced to 17.87 %, indicating that h^+ also plays an important role in the photocatalytic oxidation reaction. However, the degradation efficiency of BPA is slightly reduced after the addition of KPS (88.92 %) and BQ (84.47 %). Generally, obvious reduction of photocatalytic efficiency indicates that the corresponding substance owns an important effect.[34–36] Consequently, the results of the active substance capture experiments indicate that $^{\bullet}OH$ and h^+ are the main active substances, while $^{\bullet}O_2^-$ and e^- have minor effects on the degradation of BPA in this RE-doped CeO_2 system. Besides, SC has no significant attenuation after four cycles of BPA photooxidation degradation (Figure 5d), indicating the as-fabricated SC photocatalyst retains excellent photocatalytic stability. Meanwhile, YC, LC, NC and pure CeO_2 also maintain a good reusability.

The photooxidation activity of products was further evaluated from the photocatalytic decomposition of gaseous acetaldehyde (CH_3CHO). And the following reactions can be considered in Equations (5–9):

$$O_2 + e^- \rightarrow {}^{\bullet}O_2{}^- \tag{5}$$

$$CH_3CHO + {}^{\bullet}O_2{}^- \rightarrow CH_3CO^{\bullet} + HO_2{}^- \tag{6}$$

$$CH_3CHO + HO_2{}^- \rightarrow CH_3CO^- + H_2O_2 \tag{7}$$

$$CH_3CO^- + {}^{\bullet}OH \rightarrow CH_3COOH + e^- \tag{8}$$

$$2CH_3COOH + 4O_2 \rightarrow 4CO_2 + 4H_2O \tag{9}$$

Compared with pure CeO_2, the photocatalytic activity is clearly enhanced after RE ions doping (Figure 6a). In the case of Sm doping, the amount of CO_2 liberation reaches a maximum of about 304.05 ppm, which is 8.50-times higher than that of pure CeO_2 (35.76 ppm). The excellent photocatalytic activity is attributed to the concentration of O_v reaching a maximum value in SC, and the results are consistent with results of Raman and XPS analyses. The process of CH_3CHO decomposition follows the first-order kinetic equation obviously (Figure 6b). According to the kinetic equation, the rate constant value of SC reaches 0.3041 h^{-1} and is clearly higher than other values (YC (0.2762 h^{-1}), LC (0.1525 h^{-1}), NC (0.1128 h^{-1}), CeO_2 (0.0364 h^{-1})). The SC photocatalyst as-fabricated in this paper shows much higher activity for CH_3CHO (340 ppm) oxidation than the activities of commercial metal oxide photocatalysts such as TiO_2 (21 ppm), S-doped TiO_2 (150 ppm) and WO_3 (200 ppm).[37,38] It also shows much higher activity than the other CeO_2 photocatalysts with different morphologies including nanoparticles (200 ppm), hedgehog-like (140 ppm), confeito-like (100 ppm) and octahedral structures (80 ppm).[7–9]

The optical effect of dopant ion substitution into the CeO_2 lattice was further confirmed using UV-vis absorption spectra (Figure 7a). For semiconductors, the absorption edge of the band follows Equation (10):

$$(\alpha h\upsilon)^n = B(h\upsilon - E_g) \tag{10}$$

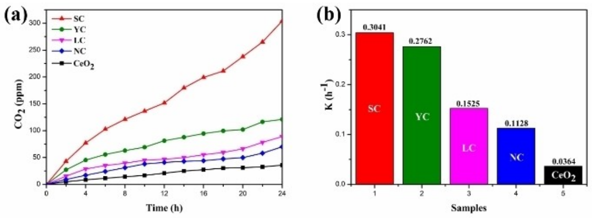

Figure 6. (a) Time course of CO_2 liberation from acetaldehyde decomposition and (b) kinetics curves of all samples.

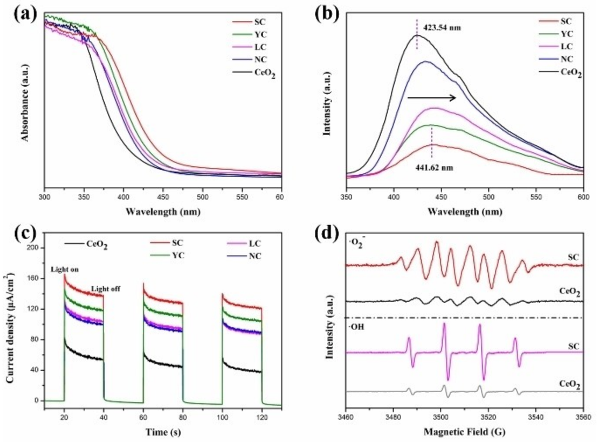

Figure 7. Photoelctrochemical characterization: (a) UV-vis diffuse reflectance spectra, (b) PL spectra, (c) transient photocurrent response curves, and (d) EPR spectra.

where α is the absorption coefficient, B is the material-related constant, hν is the discrete photon energy, E_g is the absorption bandgap, and n is the number of different types of electronic transitions.[39] It has been shown the electronic transition between the valence band and conduction band of CeO_2 is a direct transition, resulting in the value of n being 2.[40,41] The Schuster-Kubelka-Munk equation is considered to be reliable for determining a semiconductor bandgap. The band gap values of CeO_2, SC, YC, LC and NC were calculated to be 2.87, 2.59, 2.65, 2.74 and 2.79 eV, respectively (Figure S4). The results indicate that rare earth ions doping can induce narrowing of the band gap of CeO_2. A smaller band gap energy (E_g) is considered to be one of the crucial parameters for determining the final photocatalytic performance.[42] The doping of cations can favor the formation of trivalent cerium (Ce^{3+}) and create more oxygen vacancies (O_v). An increasing concentration of O_v can also result in the formation of a doping-related transition state which is closer to the conduction band (CB) and reduce the band gap energy.43 The potential of the valence band (VB) was determined from a VB-XPS spectrum (Figure S5). The results clearly revealed that the rare earth dopant was indeed incorporated into the crystal lattice of CeO_2, resulting in alteration in the electronic properties of the RE ions doping products.[39–41,43]

Photoluminescence (PL) analysis has also been frequently used to determine the recombination rate of electrons and holes (e^- and h^+). 44 Pure CeO_2 shows a strong characteristic PL peak with a value of about 423.54 nm and a weaker peak of about 441.62 nm (Figure 7b). The two peaks are both attributed to surface defects, which are usually accommodated between the O_2p valence band and the Ce4f conduction band. It is well known that the major surface defects in CeO_2 are oxygen vacancies.[45] The doped CeO_2 samples showed emission spectra with the same number of peaks. However, the intensity of the emission band was reduced for CeO_2 doped with different RE ions. SC showed the lowest PL intensity among all the RE-doped CeO_2 samples. This indicates an excellent efficiency of promoting separation of holes and electron pairs, which can efficaciously enhance the photocatalytic performance.[45]

A photocurrent-time response test was carried out to examine the interface charge separation kinetics, and the results are shown in Figure 7c. The photocurrent response curves show that the photocurrent intensity of all samples suddenly increases and decreases when the light source is turned on and off respectively, indicating their intrinsic properties of the semiconductor.[37,46] The photocurrent intensities of RE ion-doped samples (SC (142.83 μA/cm^2), YC (124.58 μA/cm^2), LC (104.68 μA/cm^2), NC (109.08 μA/cm^2)) are all higher than that of pure CeO_2 (61.21 μA/cm^2). Interestingly, the photocurrent intensity of SC reaches a maximum value that is 2.33-times greater than that of pure CeO_2. The increasing photocurrent intensity indicates that the photogenerated charge carriers in SC are much more effectively separated than those in other samples. In general, a greater intensity of the photocurrent means higher transfer efficiency of photogenerated electrons and holes, which is beneficial for the photocatalytic reactions and affords better photocatalytic performance.[16]

The EPR results (Figure 7d) further revealed the main active species. It can be clearly observed that the intensity of hydroxyl radicals ($^{\bullet}OH$) and superoxide radicals ($^{\bullet}O_2^-$) is stronger than that of pure CeO_2 after Sm doping, being in good agreement with the results of the active species trapping experiments. Actually, the formation of $^{\bullet}OH$ and $^{\bullet}O_2^-$ is important for photocatalytic reactions due to both of them are highly efficient intermediates to further promote the photocatalytic activity. Hence, SC can achieve a significant improvement in photooxidation performance.

Stoichiometric CeO_2 is known to be an insulator, and the features of the electronic density of states (DOS) calculated in Figure 8 are in agreement with previous DFT+U results. And it can be further used to revealing the modifications in electronic structure and the mechanism of light absorption. Compared with pure CeO_2, it is evident that conduction bands of RE-doped structures are shifted from a higher energy level to a lower energy level. Meanwhile, the doping energy level of SC and NC appeared obviously. This indicates a narrowed band gap may cause a reduction of photo-electron transition energy. At the same time, doping will regulate the energy band structure and extend the absorption edge of CeO_2 towards a wider light region effectively.[46] Plots of the energy band structures for fluorite-type CeO_2 and RE-doped CeO_2 are outlined in Figure S6. The energy band structures of YC and LC are similar with that of pure CeO_2, and similar values of the band gap are consistent with UV-vis results. Interestingly, it was found that new features appear in the band gaps of SC and NC (Figure S6 (b) and (e)), which are contributed to the overlap of energy levels between the states of dopants (Sm and Nd) and the O, resulting in the dopants-O binding. The exist of impurity energy levels significantly change the band structures and narrow the band gap, bringing higher light yield.

Based on all observed characterization results and the results of photocatalytic evaluation experiments, a reasonable reaction mechanism of RE ion-doped CeO_2 is proposed (Figure 9). The introduction of RE ions into the cubic fluorite structure of CeO_2 can affect its crystal structure evidently. After an incorporation of RE ions, the surface exposed cerium ions are partly substituted by those cations, resulting in a higher concentration of oxygen vacancies (O_v), which leads to a formation of doping transition states. Then more O_v can efficiently capture electrons in the conduction band (CB) and limit the recombination rate of photo-generated electrons and holes in doped-CeO_2. These transition states caused by doping can extend lifetime of photo-generated carriers during the migration process and further lead to an effective separation efficiency of photo-generated carriers. Additionally, abundant hydroxyl radicals ($^{\bullet}OH$) and superoxide radical ($^{\bullet}O_2^-$) can be generated in the VB and CB, respectively. The higher concentration of $^{\bullet}OH$ and $^{\bullet}O_2^-$ are both highly efficient intermediates with vivid oxidation ability to further react with organic compounds, leading to an outstanding enhancement of photooxidation performance. Based on the experiments of BPA degradation and of CH_3CHO decomposition, we can draw conclusions that the photocatalytic performance is apparently enhanced after different RE ions doping and SC possesses the

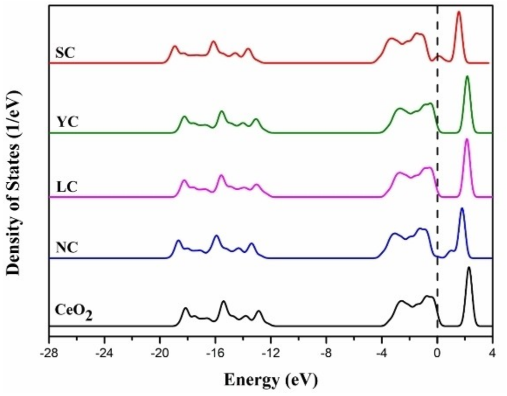

Figure 8. Density of states (DOS) of all samples.

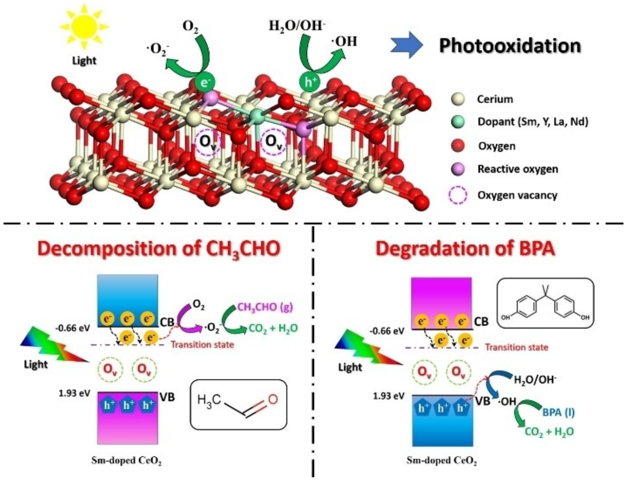

Figure 9. A proposed mechanism for photocatalytic performance enhancement.

highest photooxidation activity among them. The reasons maybe attribute to the following two factors, one is that the ionic radius of Sm^{3+} is closer to Ce^{4+}, leading to the entry of ions into the interior of the lattice much more easily and readily. The introduction of Sm ions leads to an expansion of the crystal lattice in CeO_2, which is more convenient for the transmission of electrons. And those migrated electrons can hasten the diffusion rate of oxygen and boost reactive oxygen species (ROS) effectively. The other reason is that Sm has two variable valence states and those two states will provide much more oxygen vacancies, which represents that they can further restrict the recombination rate of photogenerated carriers, then lead to an efficient promotion of the photocatalytic activity. Thus, RE ions doping is a feasible strategy to enhance the photocatalytic efficiency of traditional semiconductors.

Conclusion

In summary, CeO_2 photocatalysts doped with different RE ions were successfully prepared by a template-free hydrothermal treatment. This method for design and synthesis is cost-effective and can be easily extended to the manufacture of other RE ion-doped inorganic semiconductor materials. FE-SEM and HR-TEM images show that doped CeO_2 with a broom-like hierarchical structure is composed of numerous nanorods. Raman and XPS analyses also reveal the doped-CeO_2 has the advantage of having much more oxygen vacancies. It is found that SC exhibits superior photooxidation performance compared with that of other doped products, resulting about 3.0-times and 8.5-times higher activities than pure CeO_2 for BPA degradation and CH_3CHO decomposition, respectively. Therefore, rare earth ion-doped CeO_2 established in this paper can pave the way to fabricate other different RE ion-doped photocatalysts for energy-related and environmental remediation applications.

Experimental Section

Materials

Urea, cerium nitrate hexahydrate ($Ce(NO_3)_3 \cdot 6H_2O$), sodium citrate dihydrate ($C_6H_5O_7Na_3 \cdot 2H_2O$), yttrium nitrate hexahydrate ($Y(NO_3)_3 \cdot 6H_2O$), lanthanum nitrate hexahydrate (–$La(NO_3)_3 \cdot 6H_2O$), samarium nitrate hexahydrate ($Sm(NO_3)_3 \cdot 6H_2O$) and neodymium nitrate hexahydrate ($Nd(NO_3)_3 \cdot 6H_2O$) were used in this study. All the chemical reagents used in the experiments were of analytical grade, were commercially available with 99.9% purity and were used without further purification. Deionized water was used throughout the experiments.

Preparation

First, 5.88 g $C_6H_5O_7Na_3 \cdot 2H_2O$ was dissolved in 140 ml deionized water and the solution was stirred vigorously at room temperature for 10 min. Then 2.40 g urea was added to the solution and the solution was stirred for 30 min. The homogeneous mixture was prepared for further use. At the same time, 1.63 g $Ce(NO_3)_3 \cdot 6H_2O$ and 0.144 g rare-earth salts ($Sm(NO_3)_3 \cdot 6H_2O$, $La(NO_3)_3 \cdot 6H_2O$ $Nd(NO_3)_3 \cdot 6H_2O$ and ($Y(NO_3)_3 \cdot 6H_2O$) were dissolved in 20 ml deionized water with vigorous magnetic stirring at a room temperature for 30 min. Then aqueous solution of ceric and other rare-earth salts aqueous solution was dropped into the above mixture and stirred for 30 min until the solution changed to faint yellow color. The mixed solutions were then transferred into a 200 ml Teflon-lined autoclave and kept at 120 °C for 36 h. After cooling to room temperature naturally, a white precipitate was collected by centrifugation and washed with deionized water and ethanol at least three times each. Then RE-doped ceria was obtained by calcination of the as-prepared precursor in air at 500 °C for 4 h to collect the final faint yellow product. For simplification, samples of Sm-doped CeO_2, Y-doped CeO_2, La-doped CeO_2 and Nd-doped CeO_2 samples are denoted as SC, YC, LC and NC, respectively.

Characterization

X-ray diffraction (XRD) was performed on a Bruker-AXS X-ray focus using a Cu Ka radiation source (40 kV/40 mA). Raman spectra was obtained by an In Via Laser Confocal Raman Spectrometer. Morphology and elemental mapping of the products were observed by FE-SEM (Hitachi, S-4800) and HR-TEM (FEI, Tecnai G^2 F30S-TWIN, 300 KV). UV-vis diffuse reflectance spectra (DRS) was measured by a Varian Cary 5000 UV-vis spectrophotometer. The X-ray photoelectron spectroscopy (XPS) experiment was carried out on a Shimadzu KRATOS AXIS-NOVA system at room temperature under 10^{-9} Pa using Al $K\alpha$ radiation and C 1s peak (284.6 eV) reference. Electron paramagnetic resonance (EPR) radical signal was recorded by a Brucker EPR A200 spectrometer. Photoluminescence (PL) spectroscopy measurements were performed at an excitation wavelength of 310 nm on a fluoro-spectrophotometer (Hitachi F-4500) at room temperature.

Bisphenol A degradation experiments

Photooxidation of aqueous bisphenol A (BPA) was carried out with a 300 W UV lamp (light intensity = 100 mW/cm^2) and temperature was controlled at 25 °C. Before the experiment, 120 mg photocatalyst and 120.0 ml BPA solution (20 mg/L) were added to the reaction flask, and then an adsorption-desorption equilibrium was achieved by stirring for 1 h in a dark place. Next, the UV lamp was turned on and 4.0 mL of the suspension reaction liquid was withdrawn from the reaction flask at regular intervals. The BPA solution was separated from the photocatalyst by filtration with double layers of a cellulose acetate membrane (pore size of 0.22 μm). The concentration of BPA was measured by a UV-Vis spectrophotometer ($\lambda max = 277$ nm). The degradation products were determined by a high-performance liquid chromatograph (HPLC) equipped with a JASCO UVIDEC-100-VI optical detector and a chromatographic column of an Agilent eclipse XDB-C18 column (4.6 × 150 mm) with a column temperature of 25 °C. The eluent used was a mixed solvent of acetonitrile and water (1/1, v/v). The flow rate of the mobile phase was 1 ml/min. The elution was monitored at 277 nm.

Active species trapping experiments

In order to detect active species in the photodegradation process, potassium persulphate (KPS) was used as electron (e^-) scavenger, ethylenediaminetetraacetatic acid disodium (EDTA) was selected as hole (h^+) scavenger, tert-butanol (TBA) was employed as hydroxyl radical ($^\bullet OH$) scavenger and 1, 4-benzoquinone (BQ) was chosen as superoxide radical ($^\bullet O_2^-$) scavenger. For comparison, an experiment without a scavenger was also carried out under the same conditions. The photocatalyst with different a scavenger (1 mM) was dispersed in BPA solution (120.0 ml, 20 mg/L). The following process was same as the BPA photodegradation experiment described in experimental section 4.

Acetaldehyde decomposition experiments

Photooxidation activity for decomposition of acetaldehyde (CH_3CHO) was also assessed. One hundred mg of photocatalyst powder was spread on the bottom of a glass dish, and the glass dish was placed in a Tedlar bag (AS ONE Co., Ltd.). Then 500 ppm of CH_3CHO was injected into the bag together with 125 cm^3 of artificial air. Then the bag fabricated above was put in a dark place at room temperature for 2 h for a purpose of reaching an adsorption-desorption equilibrium. A light-emitting diode lamp (LED; Epitex, L365) was used as a light source and its intensity was controlled at 1.0 mW/cm^2, which emitted light with a central wavelength of ca. 365 nm. The concentration of generated CO_2 as a function of irradiation time was monitored by an online gas chromatograph (Agilent Technologies, 3000 A Micro-GC, TCD detector) equipped with OV1 and PLOT-Q columns.

Photoelectrochemical measurement experiments

A typical working electrode was prepared as follows: 30 mg of the photocatalyst was dispersed in 30 mL of acetone and subjected to 1-h ultrasonic treatment. Then single iodine (10 mg) was added to enhance its ionic strength and sonicated for 30 min. Next, the product was electroplated onto a 6×1 cm conductive glass (ITO) using an electrophoresis method with 15 V DC power supplied for 5 min. Finally, the ITO glass was dried at 60 °C for 10 h to obtain the film electrode. Na_2SO_4 (0.1 M) aqueous solution was used as the electrolyte. The working electrode was irradiated by a Xe arc lamp and its intensity was controlled at 100 mW/cm^2. Photoelectrochemical measurements were performed on an electrochemical analyzer (CHI660D, Shanghai, Chenhua) in a standard three-electrode configuration with Pt as the counter electrode and Ag/AgCl as a reference electrode.

Model and computational details

Density functional theory (DFT) computations were performed by using the CASTEP module as implemented in Materials Studio 8.0 (Accelrys Inc.-San Diego, USA). Both the bulk crystalline cells and the atom positions of the pristine and doped CeO_2 were optimized within the generalized gradient approximation (GGA) and the exchange-correlation functional of Perdew-Burke-Ernzerhof (PBE). The kinetic cut-off energy for the plane-wave basis set was chosen to be 470 eV, the Monkhorst-Pack k-point meshes were set as $2\times2\times5$, and the ion-electron interactions were modeled by the ultrasoft pseudo-potential. The convergence criteria of the geometry optimization for the energy change, maximum force, maximum stress, and maximum displacement tolerances were set to 2.0×10^{-5} eV/atom, 0.03 eV/Å, 0.05 GPa, and 0.001 Å, respectively. Accurate description of the electronic structure of rare elements is a well-known issue for regular DFT approaches due to the localized nature of the 4f electron. Hence, a tunable Hubbard type correction term should be included into the DFT framework: DFT+U. The value of U for Ce, Sm, Y, La, Nd was 6 eV. The super-cells used are the fluorite cubic $2\times2\times1$ cell with 48 atoms. Replacing a single Ce atom with Sm, Y, La and Nd elements results in dopant concentrations of 6.25%.

Acknowledgements

This work was supported by the Natural Science Foundation of Guangdong Province (Grant No. 2020 A151501982), the Major Projects of Nature Science Research in Universities and Colleges in Jiangsu Province, China (Grant No. 16KJA150008), the Natural Science Foundation of China (Grant No. 21805191) and the JST ACT–C program of Japan.

Conflict of Interest

The authors declare no conflict of interest.

Keywords: Doped Ceria · Hierarchical structure · Oxygen vacancies · Photooxidation

[1] N. Patel, R. Jaiswal, T. Warang, G. Scarduelli, *Appl. Catal. B* **2014**, *150*, 74–81.
[2] Y. Wang, H. Arandiyan, J. Scott, A. Bagheri, H. Dai, *J. Mater. Chem. A* **2017**, *5*, 8825–8846.
[3] H. Xu, Z. Qu, C. Zong, W. Huang, F. Quan, N. Yan, *Environ. Sci. Technol.* **2015**, *49*, 6823–6830.
[4] H. J. Kim, G. Lee, M. G. Jang, K. J. Noh, J. W. Han, *ChemCatChem* **2019**, *11*, 2288–2296.
[5] M. K. Gnanamani, G. Jacobs, W. D. Shafer, B. H. Davis, *ChemCatChem* **2017**, *9*, 492–498.
[6] B. Chen, X. Li, R. Zheng, R. Chen, X. Sun, *J. Mater. Chem. A* **2017**, *5*, 13382–13391.
[7] S. Yuán, S. Liu, Q. Zhang, M. Zhang, B. Xu, T. Ohno, *ChemCatChem* **2018**, *10*, 1–6.
[8] S. Yuan, Q. Zhang, B. Xu, Z. Jin, M. Zhang, T. Ohno, *RSC Adv.* **2014**, *4*, 62255–62261.
[9] B. Xu, Q. Zhang, S. Yuan, M. Zhang, T. Ohno, *Chem. Eng. J.* **2015**, *260*, 126–132.
[10] B. Choudhury, P. Chetri, A. Choudhury, *RSC Adv.* **2014**, *4*, 4663–4671.
[11] Y. Huang, Y. Lu, Y. Lin, Y. Mao, G. Ouyang, H. Liu, *J. Mater. Chem. A* **2018**, *6*, 24740–24747.
[12] B. Mandal, A. Mondal, S. S. Ray, A. Kundu, *Dalton Trans.* **2016**, *45*, 1679–1692.
[13] F. Dvořák, O. Stetsovych, M. Steger, E. Cherradi, I. Matolínová, *J. Phys. Chem. C* **2011**, *115*, 7496–7503.
[14] L.-W. Qian, X. Wang, H.-G. Zheng, *Cryst. Growth Des.* **2011**, *12*, 271–280.
[15] D. Channei, B. Inceesungvorn, N. Wetchakun, S. Phanichphant, *Sci. Rep.* **2014**, *4*, 5757.
[16] Y. Huang, B. Long, M. Tang, Z. Rui, M.-S. Balogun, Y. Tong, H. Ji, *Appl. Catal. B* **2016**, *181*, 779–787.
[17] X. Zhou, J. Ling, W. Sun, Z. Shen, *J. Mater. Chem. A* **2017**, *5*, 9717–9722.
[18] L. Truffault, M.-T. Ta, T. Devers, K. Konstantinov, *Mater. Res. Bull.* **2010**, *45*, 527–535.
[19] J. Saranya, K. S. Ranjith, P. Saravanan, D. Mangalaraj, R. T. Rajendra Kumar, *Mater. Sci. Semicond. Process.* **2014**, *26*, 218–224.
[20] C. Siriwong, N. Wetchakun, B. Inceesungvorn, *Prog. Cryst. Growth Charact. Mater.* **2012**, *58*, 145–163.
[21] D. Jampaiah, K. M. Tur, S. J. Ippolito, Y. M. Sabri, *RSC Adv.* **2013**, *3*, 12963.
[22] E. Sasmaz, C. Wang, M. J. Lance, J. Lauterbach, *J. Mater. Chem. A* **2017**, *5*, 12998–13008.
[23] W. L. Wang, W. Y. Liu, X. L. Weng, Y. Shang, J. J. Chen, Z. G. Chen, Z. B. Wu, *J. Mater. Chem. A* **2018**, *6*, 866–870.
[24] X. Zhang, X. Xie, H. Wang, J. Zhang, B. Pan, *J. Am. Chem. Soc.* **2013**, *135*, 18–21.
[25] Y. Lee, G. He, A. J. Akey, R. Si, M. Flytzani-Stephanopoulos, I. P. Herman, *J. Am. Chem. Soc.* **2011**, *133*, 12952–12955.
[26] S. Chang, M. Li, Q. Hua, L. Zhang, Y. Ma, B. Ye, W. Huang, *J. Catal.* **2012**, *293*, 195–204.
[27] Z. D. Dohčević-Mitrovi, M. Grujić-Brojčin, M. Šćepanović, *J. Phys. Condens. Matter* **2006**, *18*, S2061–S2068.

[28] A. Tovt, L. Bagolini, F. Dvořák, N.-D. Tran, *J. Mater. Chem. A* **2019**, *7*, 13019–13028.
[29] L. Ma, D. Wang, J. Li, B. Bai, L. Fu, Y. Li, *Appl. Catal. B* **2014**, *148*, 36–43.
[30] M. S. M. Yoon, C. Jeong, J. H. Jang, K. S. Jeon, *Chem. Mater.* **2005**, *17*, 6069–6079.
[31] R. Ma, M. Jahurul Islam, D. Amaranatha Reddy, T. K. Kim, *Ceram. Int.* **2016**, *42*, 18495–18502.
[32] S. Hu, F. Zhou, L. Wang, J. Zhang, *Catal. Commun.* **2011**, *12*, 794–797.
[33] M. J. Islam, D. A. Reddy, J. Choi, T. K. Kim, *RSC Adv.* **2016**, *6*, 19341–19350.
[34] Z. a Huang, Q. Sun, K. Lv, Z. Zhang, M. Li, B. Li, *Appl. Catal. B* **2015**, *164*, 420–427.
[35] P. Dumrongrojthanath, T. Thongtem, A. Phuruangrat, *Superlattices Microstruct.* **2013**, *54*, 71–77.
[36] F. Deng, Y. Liu, X. Luo, D. Chen, S. Wu, *Sep. Purif. Technol.* **2013**, *120*, 156–161.
[37] K. Kondo, N. Murakami, T. Tsubota, T. Ohno, *Appl. Catal. B* **2013**, *142*, 362–367.
[38] Z. Jin, N. Murakami, T. Tsubota, T. Ohno, *Appl. Catal. B* **2014**, *150*, 479–485.
[39] P. Patsalas, S. Logothetidis, L. Sygellou, S. Kennou, *Phys. Rev. B* **2003**, *68*, 035104.
[40] D. Jampaiah, S. J. Ippolito, Y. M. Sabri, B. M. Reddy, *Catal. Sci. Technol.* **2015**, *5*, 2913–2924.
[41] S. Hu, F. Zhou, L. Wang, J. Zhang, *Catal. Commun.* **2011**, *12*, 794–797.
[42] H. Yang, B. Xu, S. Yuan, Q. Zhang, M. Zhang, T. Ohno, *Appl. Catal. B* **2019**, *243*, 513–521.
[43] W. Liu, L. Cao, W. Cheng, Y. Cao, X. Liu, W. Zhang, X. Mou, L. Jin, X. Zheng, W. Che, Q. Liu, T. Yao, S. Wei, *Angew. Chem. Int. Ed.* **2017**, *56*, 9312–9317; *Angew. Chem.* **2017**, *129*, 9440–9445.
[44] N. Tian, H. Huang, C. Liu, F. Dong, T. Zhang, X. Du, S. Yu, Y. Zhang, *J. Mater. Chem. A* **2015**, *3*, 17120–17129.
[45] P. Ji, J. Zhang, F. Chen, M. Anpo, *Appl. Catal. B* **2009**, *85*, 148–154.
[46] Y. Xue, D. Tian, D. Zhang, C. Zeng, *Comput. Mater. Sci.* **2019**, *158*, 197–208.

Manuscript received: December 18, 2019
Revised manuscript received: March 8, 2020
Accepted manuscript online: March 9, 2020
Version of record online: ■■, ■■

Photocatalysis: CeO_2 doped with Sm, Y, La and Nd having a broom-like hierarchical structure was successfully synthesized. The enhanced photocatalytic activity can be attributed to a higher concentration of oxygen vacancies caused by doping. During the process of photocatalytic degradation, abundant highly reactive hydroxyl radicals ($^{\bullet}OH$) and superoxide radicals ($^{\bullet}O_2^{-}$) are efficient intermediates with vivid oxidation ability.

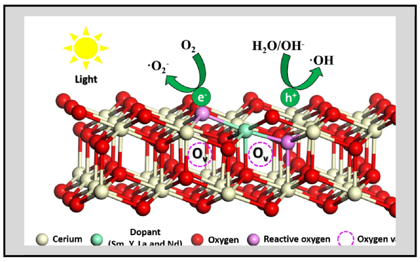

Assoc. Prof. B. Xu, H. Yang, Assoc. Prof. Q. Zhang*, S. Yuan, Assoc. Prof. A. Xie, Prof. M. Zhang, Prof. T. Ohno**

1 – 10

Design and Synthesis of Sm, Y, La and Nd-doped CeO_2 with a broom-like hierarchical structure: a photocatalyst with enhanced oxidation performance